Astronomy & Astrophysics manuscript no. ms
February 14, 2023

KMT-2021-BLG-1122L: The first microlensing triple stellar system

Cheongho Han[01], Youn Kil Jung[02], Andrew Gould[03, 04], Doeon Kim[01], Chung-Uk Lee[02]
(Leading authors)
and
Michael D. Albrow[05], Sun-Ju Chung[02], Kyu-Ha Hwang[02], Hyoun-Woo Kim[02], Yoon-Hyun Ryu[02], In-Gu Shin[06], Yossi Shvartzvald[07], Hongjing Yang[08], Jennifer C. Yee[06], Weicheng Zang[06, 08], Sang-Mok Cha[02, 09], Dong-Jin Kim[02], Seung-Lee Kim[02, 10], Dong-Joo Lee[02], Yongseok Lee[02, 09], Byeong-Gon Park[02, 10], and Richard W. Pogge[04]
(The KMTNet Collaboration)

[1] Department of Physics, Chungbuk National University, Cheongju 28644, Republic of Korea
e-mail: cheongho@astroph.chungbuk.ac.kr
[2] Korea Astronomy and Space Science Institute, Daejon 34055, Republic of Korea
[3] Max Planck Institute for Astronomy, Königstuhl 17, D-69117 Heidelberg, Germany
[4] Department of Astronomy, The Ohio State University, 140 W. 18th Ave., Columbus, OH 43210, USA
[5] University of Canterbury, Department of Physics and Astronomy, Private Bag 4800, Christchurch 8020, New Zealand
[6] Center for Astrophysics | Harvard & Smithsonian 60 Garden St., Cambridge, MA 02138, USA
[7] Department of Particle Physics and Astrophysics, Weizmann Institute of Science, Rehovot 76100, Israel
[8] Department of Astronomy and Tsinghua Centre for Astrophysics, Tsinghua University, Beijing 100084, China
[9] School of Space Research, Kyung Hee University, Yongin, Kyeonggi 17104, Republic of Korea
[10] Korea University of Science and Technology, 217 Gajeong-ro, Yuseong-gu, Daejeon, 34113, Republic of Korea

Received ; accepted

ABSTRACT

Aims. We systematically inspect the microlensing data acquired by the KMTNet survey during the previous seasons in order to find anomalous lensing events for which the anomalies in the lensing light curves cannot be explained by the usual binary-lens or binary-source interpretations.

Methods. From the inspection, we find that interpreting the three lensing events OGLE-2018-BLG-0584, KMT-2018-BLG-2119, and KMT-2021-BLG-1122 requires four-body (lens+source) models, in which either both the lens and source are binaries (2L2S event) or the lens is a triple system (3L1S event). Following the analyses of the 2L2S events presented in Han et al. (2023), here we present the 3L1S analysis of the KMT-2021-BLG-1122.

Results. It is found that the lens of the event KMT-2021-BLG-1122 is composed of three masses, in which the projected separations (normalized to the angular Einstein radius) and mass ratios between the lens companions and the primary are $(s_2, q_2) \sim (1.4, 0.53)$ and $(s_3, q_3) \sim (1.6, 0.24)$. By conducting a Bayesian analysis, we estimate that the masses of the individual lens components are $(M_1, M_2, M_3) \sim (0.47\, M_\odot, 0.24\, M_\odot, 0.11\, M_\odot)$. The companions are separated in projection from the primary by $(a_{\perp,2}, a_{\perp,3}) \sim (3.5, 4.0)$ AU. The lens of KMT-2018-BLG-2119 is the first triple stellar system detected via microlensing.

Key words. Gravitational lensing: micro – (Stars:) binaries: general

1. Introduction

Light curves of gravitational microlensing events often exhibit deviations from the smooth and symmetric form of the event involved with a single lens mass and a single source star (Paczyński 1986). The most common cause of such deviations is the binarity of the lens, 2L1S event (Mao & Paczyński 1991), or the source, 1L2S event (Griest & Hu 1993; Han & Gould 1997). Anomalous lensing events comprise about 10% of more than 3000 lensing events that are being annually detected from the three currently working lensing surveys conducted by the Optical Gravitational Lensing Experiment (OGLE: Udalski et al. 2015), Microlensing Observations in Astrophysics (MOA: Bond et al. 2001), and Korea Microlensing Telescope Network (KMTNet: Kim et al. 2016) groups. The prime goal of these survey experiments is finding extrasolar planets, which are detected via anomalous signals in lensing light curves. Planetary microlensing signals appear in various shapes and often confused with anomalies produced by other causes. In order to sort out planetary signals from those of other origins, therefore, it is essential to analyze all anomalous events.

In the current microlensing experiments, anomalous events are being analyzed almost in real time with the progress of events. This became possible with the implementation of early warning systems: the OGLE early warning system (Udalski et al. 1994), MOA real-time analysis system (Bond et al. 2001), and KMTNet EventFinder AlertFinder (Kim et al. 2018b) system.[1] These systems enable one to detect lensing events in their early phases and to promptly identify anomalies appearing in lensing light curves. Analyses of the events with identified anomalies are conducted by multi-

[1] In addition, the KMTNet EventFinder system (Kim et al. 2018a) carries out end-of-season analyses that recover many events that were missed for one reason or another by AlertFinder (Kim et al. 2018b) system.

ple modelers of the individual survey groups as the anomalies proceed, and models of the events found from these analyses are circulated or posted on web pages[2] to inform researchers in the microlensing community of the nature of the anomalies. In most cases, anomalous events are interpreted with a binary-lens (2L1S) or a binary-source (1L2S) model.

For a minor fraction of anomalous events, it is known that the anomalies cannot be explained by the usual 2L1S or 1L2S interpretation. Han et al. (2023), hereafter Paper I, conducted a systematic investigation of events found from the KMTNet survey during the previous seasons in search for anomalous events for which no plausible models had been presented. From this investigation, they found that the anomalies appearing in the light curves of the events OGLE-2018-BLG-0584 and KMT-2018-BLG-2119 required a four-body (lens+source) model, in which both the lens and source are binaries (2L2S event). In this paper, we present the analysis of another four-body lensing event KMT-2021-BLG-1122. Unlike the two 2L2S events presented in Paper I, the lens system of KMT-2021-BLG-1122 is composed of three masses (3L1S).

We present the analysis of the event KMT-2021-BLG-1122 according to the following organization. In Sect. 2, we depict the observations conducted to obtain the photometric data of the event, and describe the characteristic features of the anomaly appearing in the light curve of the event. In Sect. 3, we begin by describing the lensing parameters used in the modeling conducted under various configurations of the lens and source system, and we then describe detail of the analyses conducted under the individual configurations in the following subsections: 2L1S model in Sect. 3.1, 2L2S model in Sect. 3.2, and 3L1S model in Sect. 3.3. In Sect. 4, we specify the source star of the event and estimate the angular Einstein radius of the lens system. In Sect. 5, we estimate the physical parameters including the masses of the individual lens components, the distance to the lens system, and the projected separations among the lens components. We summarize the results from the analysis and conclude in Sect. 6.

2. Lensing light curve and observations

The lensing event KMT-2021-BLG-1122 was detected solely by the KMTNet survey. The event occurred on a faint source star, with a baseline magnitude of $I_{\rm base}$ = 20.36, located toward the Galactic bulge field with equatorial coordinates (RA, DEC) = (17:35:51.10, −28:26:47.22), which correspond to the Galactic coordinates $(l, b) = (-0^\circ.720, 2^\circ.076)$. The source lies in the KMTNet BLG14 field, toward which observations were conducted with a 1 hr cadence. The event was identified by the KMTNet AlertFinder system and an alert was issued on 2021 June 3, which corresponds to the abridged Heliocentric Julian Date of HJD′ ≡ HJD − 2450000 ∼ 9368.5.

Observations of the event were carried out with the use of the three 1.6 m telescopes operated by the KMTNet group. The telescopes are distributed in the three continents of the Southern Hemisphere for continuous coverage of lensing events, and the sites of the individual telescopes are the Siding Spring Observatory in Australia (KMTA), the Cerro Tololo Interamerican Observatory in Chile (KMTC), and the South African Astronomical Observatory in South Africa (KMTS). The camera mounted on each telescope is composed of four 9k × 9k CCD chips, which in combination yield a 4 deg^2 field of view.

[2] For example, the model page of lensing events maintained by Cheongho Han (http://astroph.chungbuk.ac.kr/~cheongho).

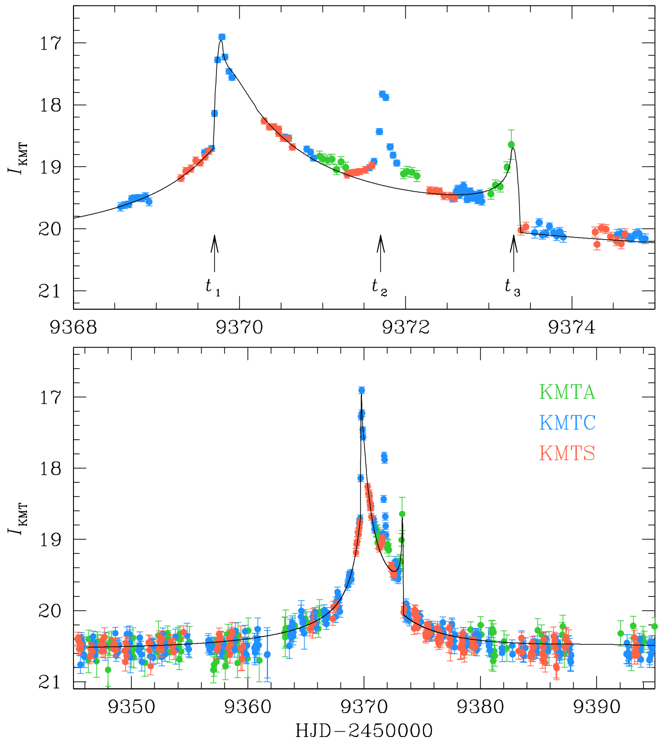


Fig. 1. Light curve of KMT-2021-BLG-1122 constructed with the combined data obtained from the three KMTNet telescopes (KMTA, KMTC, and KMTS). The curve drawn over the data points is the best-fit model found under the 2L1S interpretation. The lower panel displays the whole view, and the upper panel shows the enlarged view of the anomaly region. The epochs marked by t_1, t_2, and t_3 indicate the three major anomaly features.

Images containing the source were mainly taken in the I band, and about one tenth of images were obtained in the V band. Reductions of the images and photometry of the event were done using the KMTNet pipeline constructed based on the pySIS code of Albrow et al. (2009), and additional photometry was carried out for a subset of the KMTC data set using the pyDIA code of Albrow (2017). The analysis of the event was done based on the I-band light curve constructed from the pySIS reduction, and the pyDIA photometry data were used for the source color measurement. We discuss the detailed procedure of the source color measurement in Sect. 4. According to recipe described in Yee et al. (2012), we readjusted the error bars of the data determined by the automated pipeline in order that the errors were consistent with the scatter of data and χ^2 per degree of freedom (dof) for each data set became unity.

Figure 1 shows the lensing light curve of KMT-2021-BLG-1122 constructed with the combined I-band pySIS photometry data obtained from the three KMTNet telescopes. It shows a strong anomaly relative to a 1L1S form, and the anomaly displays a complex pattern that is characterized by the three strong features appearing at HJD′ ∼ 9369.7 (t_1), ∼ 9371.7 (t_2), and ∼ 9373.3 (t_3). From the characteristic profiles described in Schneider & Weiss (1986), the anomalies at around t_1 and t_3 appear to be a pair of caustic-crossing features produced when a source enters and exits a caustic, respectively. On the other hand, the profile at around t_2, which is approximately symmetric with respect to the peak, appears to be produced when a source approaches close to or crosses over the cusp of a caustic (Schneider & Weiss 1987).

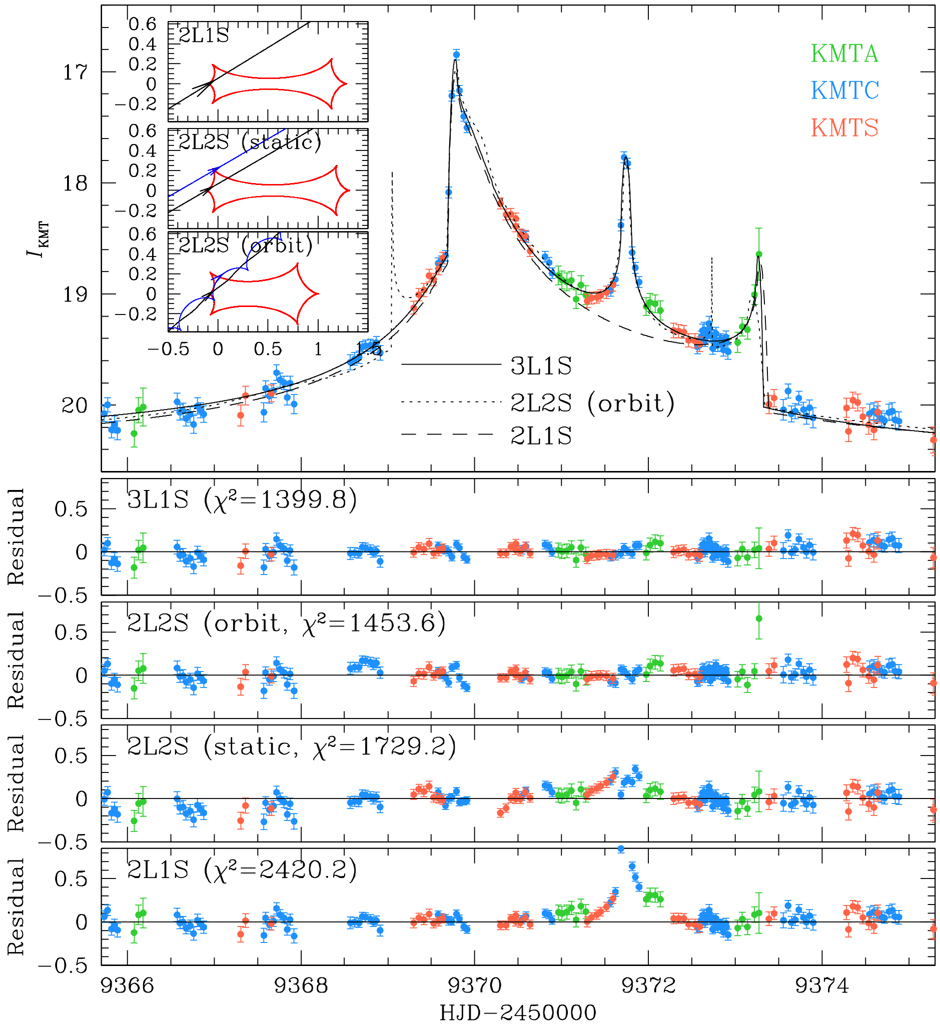


Fig. 2. Enlarged view around the central anomaly region of the light curve. Three model curves obtained under the 3L1S, 2L2S, and 2L1S lens-system configurations are drawn over the data points, and the three lower panels show the residuals from the individual models. The two insets in the top panel show the lens-system configurations of the 2L1S and 2L2S models. In each inset, the red figure is the caustic and the line with an arrow represents the source trajectory. For the 2L2S configuration, there are two source trajectories, in which the black and blue ones represent the trajectories of the primary and secondary source stars, respectively.

In general, the light curve profile of a 2L1S event in the region between a pair caustic-crossing spikes exhibits a "U"-shape pattern. Occasionally, deviations from this U-shape pattern can arise if a source sweeps one fold of a caustic, for example, OGLE-2016-BLG-0890 (Han et al. 2022c), but, in this case, the resulting deviation is smooth and thus differs from the sharp pattern of the observed anomaly at around t_2. This suggests that a different explanation is needed to explain the origin of the anomaly.

3. Interpreting the anomaly

In order to explain the anomalies in the lensing light curve, we conducted a series of modeling under various interpretations of the lens-system configuration. We tested three models under the 2L1S, 2L2S, and 3L1S configurations. We exclude 1L2S and 1L3S models because the observed light curve exhibits obvious caustic-crossing features, that is, those around t_1 and t_3, while 1L2S and 1L3S events do not involve caustics.[3]

[3] There has been only one 1L3S microlensing event published to date: OGLE-2015-BLG-1459 (Hwang et al. 2018).

In the modeling under each tested interpretation, we search for a lensing solution, representing a set of lensing parameters that characterize the observed lensing light curve. The basic lensing parameters of a 1L1S event include (t_0, u_0, t_E), which denote the time of the closest source approach to the lens, the source-lens separation (impact parameter) at t_0, and the Einstein time scale, respectively. The Einstein time scale represents the time required for the source to transit the angular Einstein radius of the lens, θ_E, and the length of u_0 is scaled to θ_E.

A 2L1S system corresponds to the case in which the lens contains an extra component compared to the 1L1S system. Consideration of the extra lens component requires one to include additional parameters in modeling. These additional parameters are (s, q, α, ρ), and they denote the projected separation (normalized to θ_E), and mass ratio between the lens components (M_1 and M_2), the angle (source trajectory angle) between the relative lens-source proper motion, $\boldsymbol{\mu}$, and the axis connecting M_1 and M_2, and the ratio between the angular radius of the source, θ_*, to the Einstein radius, that is, $\rho = \theta_*/\theta_E$ (normalized source radius), respectively. The normalized source radius is included in modeling because a 2L1S event usually involves caustic cross-

ings, during which lensing magnifications are affected by finite-source effects (Bennett & Rhie 1996). For the computation of finite-source magnifications, we utilize the map-making method of Dong et al. (2008).

For the modeling of a 2L2S system, it is required to include extra parameters in addition to those of the 2L1S model in order to describe an extra source. These extra parameters include $(t_{0,2}, u_{0,2}, \rho_2, q_F)$, where the first three denote the closest approach time, impact parameter, and normalized radius of the source companion, and the last parameter indicates the flux ratio between the companion (S_2) and primary (S_1) of the source. In the 2L2S modeling, we use the notations $(t_{0,1}, u_{0,1}, \rho_1)$ to denote the parameters related to S_1.

A 3L1S system has an extra lens component (M_3) compared to the 2L1S system, and this requires one to include additional parameters in modeling. These parameters include (s_3, q_3, ψ), which denote the separation and mass ratio between M_1 and M_3, and the orientation angle of M_3 as measured from the M_1–M_2 axis with a center at the position of M_1, respectively. In order to distinguish the parameters describing M_2 from those describing M_3, we use the notations (s_2, q_2) to denote the separation and mass ratio of M_2. The lensing parameters for the 1L1S, 2L1S, 2L2S, and 3L1S models are summarized in Table 1 of Paper I.

3.1. 2L1S interpretation

We started with modeling the light curve under the 2L1S interpretation of the anomalies. In this modeling, we searched for the binary parameters s and q via a grid approach, while we seek the other parameters via a downhill approach using a Markov Chain Monte Carlo (MCMC) algorithm. We first constructed a $\Delta\chi^2$ map on the plane of the grid parameters, identified local minima, and then refined the individual minima by allowing all lensing parameters to vary. From the 2L1S modeling, we found no lensing solution that could describe all the anomaly features, and this explains why the event had been left without a plausible model.

Although the light curve could not be explained by a 2L1S model, we found a solution that could approximately describe the caustic-crossing features at around t_1 and t_3. The model curve of this solution, found from modeling the light curve with the exclusion of the data around t_2, is drawn over the data points in Figures 1 and 2, and the corresponding configuration of the lens system is presented in the upper inset of the top panel of Figure 2. The binary lensing parameters of the solution are $(s, q) \sim (1.69, 0.43)$, which results in a single resonant caustic elongated along the binary axis. According to this solution, the source entered the caustic by crossing the caustic fold lying just above the left side on-axis cusp, passed through the inner region of the caustic, and then exited the caustic by crossing the upper fold of the caustic. The caustic entrance and exit resulted in the anomaly features matching well the observed ones around t_1 and t_3, respectively.

3.2. 2L2S interpretation

The fact that the two caustic-crossing features can be described by a 2L1S model suggests that the other anomaly feature around t_2 may be explained with the introduction of an extra source (2L2S) or an extra lens component (3L1S) to the 2L1S configuration. In this section, we present the analysis conducted under the 2L2S interpretation.

Table 1. Lensing parameters of the 2L2S solutions

Parameter	Static	Orbital
χ^2/dof	1729.1/1426	1453.6/1429
$t_{0,1}$ (HJD′)	9371.208 ± 0.026	9370.681 ± 0.007
$u_{0,2}$	0.057 ± 0.002	0.044 ± 0.001
$t_{0,2}$ (HJD′)	9370.810 ± 0.024	–
$u_{0,2}$	0.194 ± 0.004	–
t_E (days)	14.36 ± 0.31	14.87 ± 0.11
s	1.723 ± 0.020	1.447 ± 0.006
q	0.649 ± 0.043	0.261 ± 0.002
α (rad)	2.615 ± 0.009	2.415 ± 0.005
s_s	–	0.079 ± 0.001
q_s	–	0.103 ± 0.001
ϕ (rad)	–	1.326 ± 0.012
ds_s/dt (yr^{-1})	–	−0.064 ± 0.031
$d\phi/dt$ (deg/day)	–	53.79 ± 0.30
ρ_1 (10^{-3})	3.29 ± 0.17	4.58 ± 0.05
ρ_2 (10^{-3})	2.23 ± 0.79	0.10 ± 0.01
q_F	0.71 ± 0.05	0.15 ± 0.01

Notes. HJD′ = HJD − 2450000.

The 2L2S modeling was carried out based on the 2L1S solution. With the initial parameters obtained from the 2L1S modeling, we searched for a 2L2S solution by testing various trajectories of the second source considering the location and magnitude of the anomaly around t_2. We first check the case in which the position of the source companion with respect to the primary source does not vary: "static 2L2S model". The model curve of the best-fit static 2L2S solution is presented in Figure 2, and the lensing parameters are listed in Table 1. The lens-system configuration of the solution is shown in the middle inset of the top panel. The caustic configuration is similar to that of the 2L1S solution except that there are two source trajectories of S_1 and S_2, which are marked by black and blue arrowed lines, respectively. According to the solution, the source companion approached the lens slightly earlier than the primary source with an impact parameter greater than that of the primary source. The second source passed the tip of the upper left caustic cusp, and this produced the anomaly feature around t_2. Although the static 2L2S model can give rise to a sharp anomaly features appearing in the inner region between the caustic spikes, it was found that the residual from the 2L2S model was substantial, as shown in the second lower panel of Figure 2.

We further check whether the anomalies can be explained by considering the orbital motion of the source: "orbital 2L2S model". We consider the source orbital motion by introducing five extra parameters of (s_s, q_s, ϕ, ds_s/dt, $d\phi/dt$), where s_s and q_s represent the normalized separations and mass ratio between the source components, respectively, ϕ is the orientation angle of S_2 with respect to S_1, and $(ds_s/dt, d\phi/dt)$ represent the change rates of the s_s and ϕ induced by the source orbital motion, respectively. It is found that the consideration of the source orbital motion substantially improves the fit, by $\Delta\chi^2 = 275.5$, with respect to the static model. The model curve of the best-fit orbital 2L2S solution is drawn in the top panel of Figure 2, residual is shown in the panel labeled "2L2S (orbit)", and the lensing parameters are listed in Table 1. According to the model, the anomaly features around t_1 and t_3 were produced by the primary source as is in the static case, and the feature around t_2 was produced by the secondary source. We note that the secondary source crossed the caustic two more times at HJD′ ∼ 9368.7 (t_0) and ∼ 9372.7, and the former crossing is not covered by the data and the latter crossing feature is difficult to identify in the data.

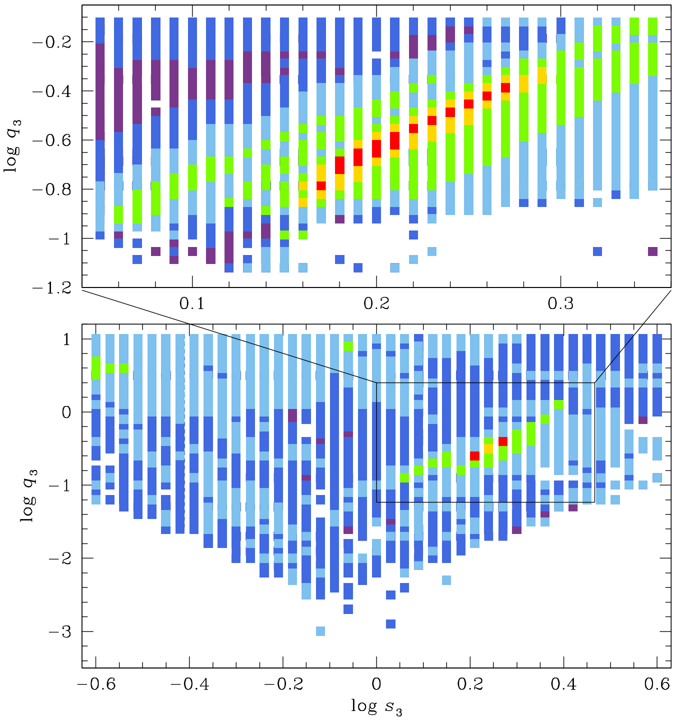


Fig. 3. Map of $\Delta\chi^2$ on the log s_3–log q_3 parameter plane obtained from the initial grid searches for (s_3, q_3) parameters. Color coding is set to represent points with $\leq 1n\sigma$ (red), $\leq 2n\sigma$ (yellow), $\leq 3n\sigma$ (green), $\leq 4n\sigma$ (cyan), $\leq 5n\sigma$ (blue), and $\leq 6n\sigma$ (purple), where $n = 9$. The upper panel shows the map around the minima constructed with denser grids.

Table 2. Lensing parameters of the best-fit 3L1S solution

Parameter	Value
χ^2/dof	1399.8/1425
t_0 (HJD′)	9370.226 ± 0.061
u_0	0.126 ± 0.008
t_E (days)	14.74 ± 0.93
s_2	1.386 ± 0.027
q_2	0.526 ± 0.039
α (rad)	2.292 ± 0.013
s_3	1.601 ± 0.043
q_3	0.241 ± 0.027
ψ (rad)	1.383 ± 0.010
ρ (10^{-3})	2.50 ± 0.21

Notes. HJD′ = HJD − 2450000.

We note that the source radius ratio $\rho_2/\rho_1 = 1/46$ and the source flux ratio $q_F = 0.15$ would lead to inconsistent estimates of θ_E, which would argue against the physical plausibility of this solution. However, we do not pursue this issue because this solution will prove to be heavily disfavored by χ^2. See Sect. 3.3.

3.3. 3L1S interpretation

We additionally searched for a model under the 3L1S interpretation. Similar to the case of the 2L2S modeling, the 3L1S modeling was done based on the 2L1S solution, from which we adopted the initial parameters of $(t_0, u_0, t_E, s_2, q_2, \alpha, \rho)$. We then conducted preliminary searches for the parameters related to M_3, that is, (s_3, q_3, ψ), via a grid approach, and finally refined the solution by letting all parameters vary. Figure 3 shows the $\Delta\chi^2$ map on the log s_3–log q_3 parameter plane constructed from the preliminary grid search. The map shows that there exists a unique χ^2 minimum at (log s_3, log q_3) ∼ (0.2, −0.6).

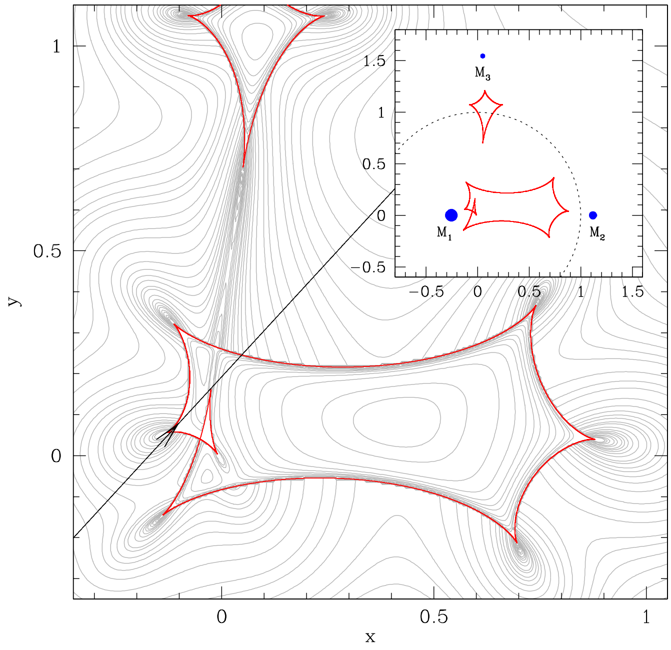


Fig. 4. Lens-system configuration of the 3L1S model. The main panel shows the central anomaly region, and the inset displays the whole view of the lens system, where blue dots marked by M_1, M_2, and M_3 denote the positions of the individual lens components. Grey curves around the caustic represent the equi-magnification contours. The dotted circle centered at the origin of the coordinates represents the Einstein ring of the lens system.

It was found that the model identified under the 3L1S interpretation well described all the observed anomaly features in the lensing light curve. The lensing parameters of the best-fit 3L1S solution are listed in Table 2 together with the value of χ^2/dof. In Figure 2, we draw the model curve (solid curve drawn over the data points) and residual (presented in the panel labeled "3L1S") from the model. The parameters related to M_2 and M_3 are $(s_2, q_2) \sim (1.4, 0.53)$ and $(s_3, q_3) \sim (1.60, 0.24)$, respectively, indicating that the primary of the lens is accompanied by two lower-mass companions lying in the vicinity of the Einstein ring. If the separations among the lens components were intrinsic (3-dimensional), the three-body lens system would be dynamically unstable, and this indicates that one or both companions are likely to be aligned by chance with the primary. We found that it was difficult to detect microlens-parallax effects (Gould 1992) due to the relatively short time scale, $t_E \sim 15$ days, of the event compared to the orbital period of Earth.

The lens-system configuration of the 3L1S model is shown in Figure 4, in which the main panel shows the central anomaly region and the inset shows the whole view of the lens system. The coordinates of the configuration is centered at the effective position of the M_1–M_2 pair defined by Di Stefano & Mao (1996) and An & Han (2002), and the grey curves encompassing the caustic represent the equi-magnification contours. One finds that the caustic induced by M_2 is similar to that of the 2L1S solution, but the 3L1S caustic and the resulting magnification pattern around the caustic are distorted by M_3, which makes the central part of the caustic nested and self-intersected (Gaudi et al. 1998; Daněk & Heyrovský 2015a,b, 2019). According to the 3L1S solution, the anomaly appearing around t_2 was produced by the

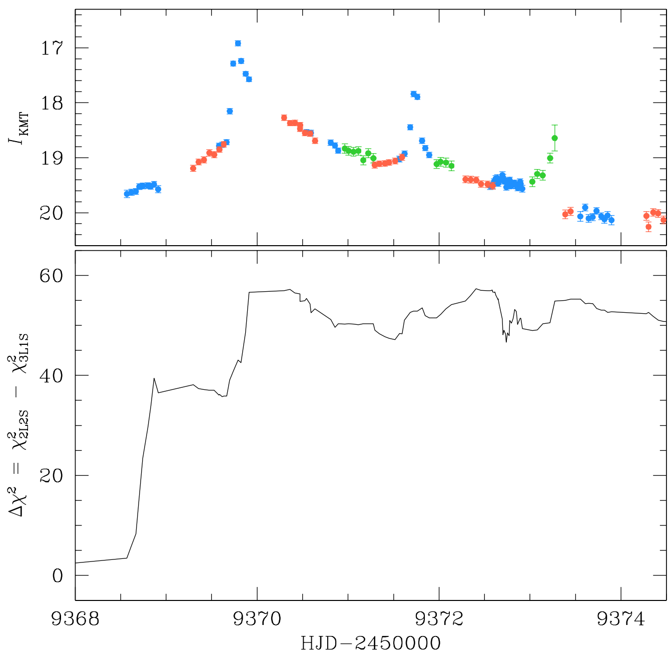


Fig. 5. Cumulative distribution of the χ^2 difference, $\Delta\chi^2 = \chi^2_{\rm 2L2S} - \chi^2_{\rm 3L1S}$, between the 2L2S (orbital) and 3L1S models in the region of the major anomaly. The light curve in the upper panel is shown to indicate the epochs of major χ^2 differences.

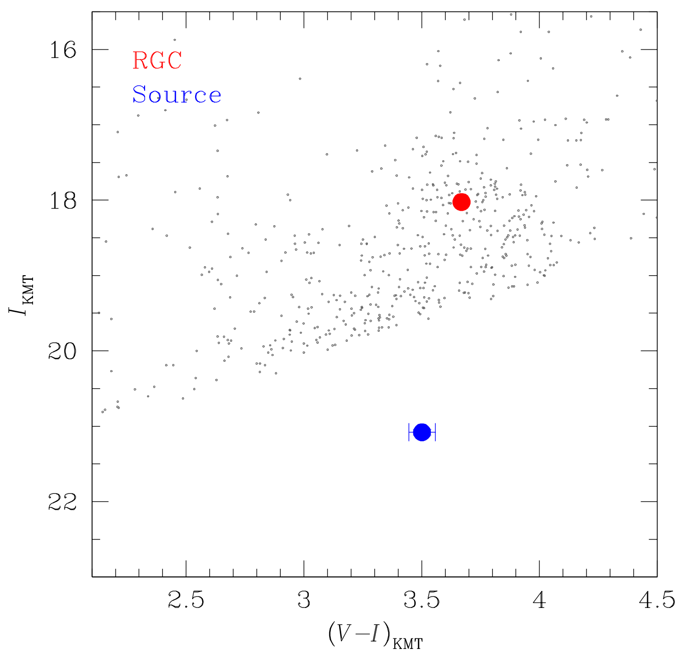


Fig. 6. Position of the source (blue dot) with respect to the centroid of red giant clump (RGC, red dot) in the instrumental color-magnitude diagram of stars lying in the vicinity of the source.

source approach close to the tip of the swallow-tail caustic part induced by M_3.

From the comparison of the 3L1S and 2L2S (orbital) models, we find that the anomaly features in the lensing light curve are better explained by the 3L1S interpretation than by the 2L2S interpretation. In Figure 5, we present the cumulative distribution of the χ^2 difference, $\Delta\chi^2 = \chi^2_{\rm 2L2S} - \chi^2_{\rm 3L1S}$, between the two models in the region of the anomaly for the detailed comparison of the two models. The major differences occur around t_0 and t_1, at around which S_2 and S_1 first crossed the caustic according to the 2L2S model, respectively. Besides these regions, the 3L1S model well explains the KMTA data point at the epoch of HJD′ = 9373.272, while the residual of this data point from the 2L2S model, $\Delta I = 0.656$ mag, is very big. As a whole, the 3L1S model yields a better fit than the 2L2S model by $\Delta\chi^2 = 53.8$, despite the fact that the 3L1S model has 4 fewer parameters.

4. Source star and Einstein radius

We specify the source of the event not only for the full characterization of the event but also for the estimation of the angular Einstein radius. The Einstein radius is determined from the angular radius of the source, θ_*, by the relation

$$\theta_{\rm E} = \frac{\theta_*}{\rho}, \quad (1)$$

where θ_* is deduced from the source type, and the normalized source radius ρ is measured from the modeling by analyzing the caustic-crossing parts of the light curve.

We determined the source type by measuring the extinction- and reddening-corrected color and brightness, $(V - I, I)_{0,S}$. For this, we utilize the Yoo et al. (2004) method, in which the source is located in the instrumental color-magnitude diagram (CMD), and then its color and magnitude are calibrated using the centroid of the red giant clump (RGC) as a reference. The RGC centroid can be used as a reference for calibration because its de-reddened color and magnitude are known.

Figure 6 shows the position of the source in the instrumental CMD constructed from the pyDIA photometry of stars lying around the source. We note that the CMD shows only bright stars due to the severe extinction, $A_I = 3.3$, toward the field. The measured instrumental color and magnitude of the source are

$$(V - I, I)_S = (3.501 \pm 0.056, 21.080 \pm 0.037), \quad (2)$$

where the I and V-band magnitudes were estimated by regressing the KMTC light curve data of the individual passbands processed using the same pyDIA code with respect to the model. By measuring the offsets in the color and magnitude, $\Delta(V - I, I)$, of the source from the RGC centroid, with $(V - I, I)_{\rm RGC} = (3.669, 18.025)$, together with the known de-reddened color and magnitude of the RGC centroid, $(V - I, I)_{0,{\rm RGC}} = (1.060, 14.377)$ (Bensby et al. 2013; Nataf et al. 2013), the de-reddened source color and magnitude were measured as

$$\begin{aligned}(V - I, I)_{0,S} &= (V - I, I)_{0,{\rm RGC}} + \Delta(V - I, I) \\ &= (0.892 \pm 0.056, 17.432 \pm 0.037).\end{aligned} \quad (3)$$

The estimated color and magnitude indicate that the source is a subgiant star of an early K spectral type.

The angular source radius was deduced from the measured source color and magnitude. For this, we first converted $V - I$ color into $V - K$ color using the color-color relation of Bessell & Brett (1988), and then estimated the angular source radius using the relation between $(V - K, V)$ and θ_* of Kervella et al. (2004). This procedure yielded the angular radii of the source and Einstein ring of

$$\theta_* = (1.26 \pm 0.11)\,\mu{\rm as}. \quad (4)$$

and

$$\theta_{\rm E} = \frac{\theta_*}{\rho} = (0.50 \pm 0.06)\,{\rm mas}, \quad (5)$$

respectively. Together with the measured event time scale, the relative lens-source proper motion was estimated as

$$\mu = \frac{\theta_E}{t_E} = (12.49 \pm 1.53)\ \mathrm{mas\ yr^{-1}}. \quad (6)$$

5. Physical lens parameters

In this section, we estimate the physical lens parameters of the mass M and distance D_L to the lens. These parameters can be sometimes constrained by measuring lensing observables of (t_E, θ_E, π_E), where π_E denotes the microlens parallax. The first two observables are related to the physical parameters by

$$t_E = \frac{\theta_E}{\mu}; \qquad \theta_E = (\kappa M \pi_{rel})^{1/2}, \quad (7)$$

where $\kappa = 4G/(c^2\mathrm{AU}) \simeq 8.14\ \mathrm{mas}/M_\odot$ and $\pi_{rel} = \pi_L - \pi_S = \mathrm{AU}(1/D_L - 1/D_S)$ represents the relative lens-source parallax. With the additional measurement of the observable π_E, the physical parameters can be uniquely constrained by the relations (Gould 2000)

$$M = \frac{\theta_E}{\kappa \pi_E}; \qquad D_L = \frac{\mathrm{au}}{\pi_E \theta_E + \pi_S}. \quad (8)$$

For KMT-2021-BLG-1122, the observables t_E and θ_E were securely measured, but the other observable π_E could not be measured, and thus we estimate the physical lens parameters by conducting a Bayesian analysis using a Galactic model together with the constraints provided by the measured observables.

In the first step of the Bayesian analysis, a large number of artificial lensing events were produced from a Monte Carlo simulation. For each simulated event, we derived the locations of the lens and source and their transverse velocity from a Galactic model, and assigned the lens mass from a mass-function model. In the Monte Carlo simulation, we adopted the Galactic model of Jung et al. (2021), whose detailed description are given therein. With the simulated events, we then constructed the posteriors of the lens mass and distance by giving a weight to each simulated event of

$$w_i = \exp(-\chi_i^2/2); \qquad \chi_i^2 = \frac{(t_{E,i} - t_E)^2}{[\sigma(t_E)]^2} + \frac{(\theta_{E,i} - \theta_E)^2}{[\sigma(\theta_E)]^2}, \quad (9)$$

where (t_E, θ_E) and $[\sigma(t_E), \sigma(\theta_E)]$ represent the measured values of the observables and their uncertainties, respectively, and $(t_{E,i}, \theta_{E,i})$ indicate the observables of each simulated event.

Figure 7 shows the posteriors of the primary lens mass (top panel), and distances to the lens (middle panel) and source (bottom panel). We additionally present the D_S posterior to show the relative location of the lens and source. For each posterior, we mark the contributions by the disk and bulge lens populations with curves drawn in blue and red, respectively. The masses of the individual lens components estimated from the Bayesian analysis are

$$M_1 = 0.47^{+0.24}_{-0.33}\ M_\odot, \quad (10)$$

$$M_2 = 0.24^{+0.13}_{-0.17}\ M_\odot, \quad (11)$$

and

$$M_3 = 0.11^{+0.06}_{-0.08}\ M_\odot. \quad (12)$$

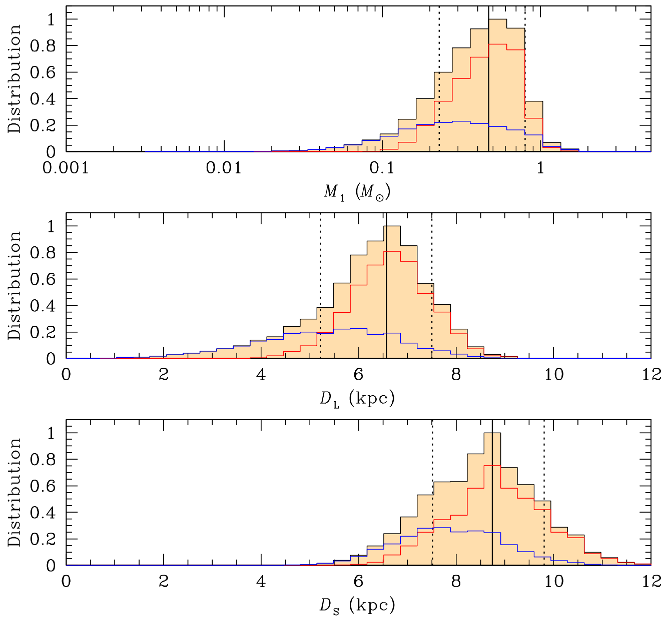


Fig. 7. Posteriors of the primary lens mass (top panel) and distance to the lens (middle panel) and source (bottom panel). In each panel, the blue and red curves represent the contributions by the disk and bulge lens populations, respectively, and the black curve is sum of the two lens populations. The solid vertical line indicates the median value, and the two dotted lines represent the 1σ range of the distribution.

The estimated masses of all the lens components are in the mass regime of M dwarfs, and thus the lens is a triple system composed of three low-mass stars. The estimated distance to the lens system is

$$D_L = 6.57^{+1.34}_{-0.94}\ \mathrm{kpc}, \quad (13)$$

and the probabilities for the lens to be in the disk and bulge are 33% and 67%, respecively. For each parameter, we present the median as a representative value and the lower and upper limits are estimated as the 16% and 84% ranges of the posterior distribution. The projected separations of the secondary and tertiary lens components from the primary are

$$a_{\perp,2} = s_2 D_L \theta_E = 3.47^{+0.71}_{-0.50}\ \mathrm{AU}, \quad (14)$$

and

$$a_{\perp,3} = s_3 D_L \theta_E = 4.01^{+0.82}_{-0.57}\ \mathrm{AU}, \quad (15)$$

respectively. As noted, the fact that the projected separations $a_{\perp,2}$ and $a_{\perp,3}$ are similar to each other suggests that one or both lens companions are aligned by chance with the primary.

We note that KMT-2021-BLG-1122L is the first triple stellar system detected via microlensing. In total, there exist 12 confirmed 3L1S events: OGLE-2006-BLG-109 (Gaudi et al. 2008; Bennett et al. 2010), OGLE-2012-BLG-0026 (Han et al. 2013), OGLE-2018-BLG-1011 (Han et al. 2019), OGLE-2019-BLG-0468 (Han et al. 2022d), OGLE-2021-BLG-1077 (Han et al. 2022a), OGLE-2006-BLG-284 (Bennett et al. 2020), OGLE-2007-BLG-349 (Bennett et al. 2016), OGLE-2008-BLG-092 (Poleski et al. 2014), OGLE-2013-BLG-0341 (Gould et al. 2014), OGLE-2018-BLG-1700 (Han et al. 2020b), KMT-2019-BLG-1715 (Han et al. 2021a), and KMT-2020-BLG-0414

(Zang et al. 2021).[4] Among them, the lenses of the first 5 events are two-planet systems, and the lenses of the other 7 events are binary-star systems possessing planets. Therefore, the common trait of the previously discovered microlensing triple systems is that at least one of the lens components is a planet. Two planets with similar separations from a host can be dynamically stable if the planets are in mean-motion resonance (Madsen & Zhu 2019). A planet in a binary system can be dynamically stable if the planet orbits one star of a wide binary stellar system or the barycenter of a closely-spaced binary system. Microlensing detection of a triple stellar system is difficult because a system with similar masses and intrinsic separations among the components would be dynamically unstable. One way for such a system to be detected via microlensing is that the companions of the triple system are closely aligned with the primary so that they lie around the Einstein ring of the primary. This alignment requires projection effect of a low probability, and this explains the relative rareness of triple stellar systems detected by microlensing.

6. Summary and conclusion

We presented the analysis of the microlensing event KMT-2021-BLG-1122, which was investigated as a part of the project to analyze anomalous lensing events in the previous KMTNet data with no suggested plausible models. We confirmed that the light curve, characterized by three major anomaly features, of the event could not be explained with the usual 2L1S or 1L2S interpretations, but it was found that a 2L1S solution obtained from the modeling with the exclusion of the data around the second anomaly feature could approximately describe the other two caustic-crossing features.

We found that all the anomaly features could be explained by introducing a tertiary lens component, and thus the lens is a triple system. The masses of the individual lens components estimated from the Bayesian analysis are $(M_1, M_2, M_3) \sim (0.47\, M_\odot, 0.24\, M_\odot, 0.11\, M_\odot)$, and the companions are separated in projection from the primary by $(a_{\perp,2}, a_{\perp,3}) \sim (3.5, 4.0)$ AU. The estimated masses of all the lens components are in the mass regime of M dwarfs, and thus the lens is a triple system composed of three low-mass stars. This is the first triple stellar-lens system detected via microlensing.

Acknowledgements. Work by C.H. was supported by the grants of National Research Foundation of Korea (2020R1A4A2002885 and 2019R1A2C2085965). J.C.Y. acknowledges the support from NSF Grant No. AST-2108414. W.Z. and H.Y. acknowledge the support by the National Science Foundation of China (Grant No. 12133005). Y.S. acknowledges support from BSF Grant No. 2020740. This research has made use of the KMTNet system operated by the Korea Astronomy and Space Science Institute (KASI) and the data were obtained at three host sites of CTIO in Chile, SAAO in South Africa, and SSO in Australia.

[4] Besides these confirmed cases, there are 6 candidate triple-lensing events, including OGLE-2014-BLG-1722 (Suzuki et al. 2018), OGLE-2018-BLG-0532 (Ryu et al. 2020), KMT-2019-BLG-1953 (Han et al. 2022a), KMT-2019-BLG-0304 (Han et al. 2021b), OGLE-2019-BLG-1470 (Kuang et al. 2022), and KMT-2021-BLG-0240 (Han et al. 2022b). For these events, 3L1S interpretations yielded best-fit models, but the signals of the tertiary lens components were not firmly confirmed either due to the subtlety of the signals or the degeneracy with other interpretations. Under the 3L1S interpretations of these events, the lenses belong to either the category of two-planet systems or the category of planets in binaries similar to the cases of the confirmed 3L1S events.

References

Albrow, M. 2017, MichaelDAlbrow/pyDIA: Initial Release on Github,Versionv1.0.0, Zenodo, doi:10.5281/zenodo.268049
Albrow, M., Horne, K., Bramich, D. M., et al. 2009, MNRAS, 397, 2099
An, J. H., & Han, C. 2002, ApJ, 573, 351
Beaulieu, J.-P., Bennett, D. P., Batista, V., et al. 2016, ApJ, 824, 83
Bennett, D. P., & Rhie, S. H. 1996, ApJ, 472, 660
Bennett, D. P., Rhie, S. H., Nikolaev, S., et al. 2010, ApJ, 713, 837
Bennett, D. P., Rhie, S. H., Udalski, A., et al. 2016, AJ, 152, 125
Bennett, D. P., Udalski, A., Bond, I. A., et al. 2020, AJ, 160, 72
Bensby, T., Yee, J. C., Feltzing, S., et al. 2013, A&A, 549, A147
Bond, I. A., Abe, F., Dodd, R. J., et al. 2001, MNRAS, 327, 868
Bessell, M. S., & Brett, J. M. 1988, PASP, 100, 1134
Daněk, K., & Heyrovský, D. 2015a, ApJ, 806, 63
Daněk, K., & Heyrovský, D. 2015b, ApJ, 806, 99
Daněk, K., & Heyrovský, D. 2019, ApJ, 880, 72
Di Stefano, R., & Mao, S. 1996, ApJ, 457, 93
Dong, S., DePoy, D. L., Gaudi, B. S., et al. 2006, ApJ, 642, 842
Gaudi, B. S., Bennett, D. P., Udalski, A., et al. 2008, Science, 319, 927
Gaudi, B. S., Naber, R. M., & Sackett, P. D. 1998, ApJ, 502, L33
Gould, A. 1992, ApJ, 392, 442
Gould, A. 1992, ApJ, 542, 785
Gould, A., Udalski, A., Shin, I. -G., et al. 2014, Science, 345, 46
Griest, K., & Hu, W. 1993, ApJ, 407, 440
Han, C., Bennett, D. P., Udalski, A., et al. 2019, AJ, 158, 114
Han, C., & Gould, A. 1997, ApJ, 480, 196
Han, C., Gould, A., Bond, I. A., et al. 2022a, A&A, 662, A70
Han, C., Kim, D., Jung, Y. K. 2020a, AJ, 160, 17
Han, C., Kim, D., Yang, H. 2022b, A&A, 664, 114
Han, C., Lee, C.-U., Gould, A., et al. 2023, A&A, in press
Han, C., Lee, C.-U., Udalski, A., et al. 2020b, AJ, 159, 48
Han, C., Ryu, Y.-H., Shin, I.-G., et al. 2022c, A&A, 667, A64
Han, C., Udalski, A., Choi, J.-Y., et al. 2013, ApJ, 762, L28
Han, C., Udalski, A., Kim, D., et al. 2021a, AJ, 161, 270
Han, C., Udalski, A., Lee, C.-U. 2021b, AJ, 162, 203
Han, C., Udalski, A., Lee, C.-U. 2022d, A&A, 658, A93
Hwang, K. -H., Udalski, A., Shvartzvald, Y., et al. 2018, AJ, 155, 20
Jung, Y. K., Han, C., Udalski, A., et al. 2021, AJ, 161, 293
Kervella, P., Thévenin, F., Di Folco, E., & Ségransan, D. 2004, A&A, 426, 29
Kim, D.-J., Kim, H.-W., Hwang, K.-H., et al. 2018a, AJ, 155, 76
Kim, H.-W., Hwang, K.-H., Shvartzvald, Y., et al. 2018b, arXiv:1806.07545
Kim, S.-L., Lee, C.-U., Park, B.-G., et al. 2016, JKAS, 49, 37
Kuang, R., Zang, W., Jung, Y. K., et al. 2022, MNRAS, 516, 1704
Madsen, S., & Zhu, W. 2019, ApJ, 878, L29
Mao, S., & Paczyński, B., 1991, ApJ, 374, L37
Nataf, D. M., Gould, A., Fouqué, P., et al. 2013, ApJ, 769, 88
Paczyński, B. 1986, ApJ, 301, 503
Poleski, R., Skowron, J., Udalski, A., et al. 2014, ApJ, 795, 42
Ryu, Y.-H., Udalski, A., Yee, J. C., et al. 2020, AJ, 160, 183
Schneider, P., & Weiss, A. 1986, A&A, 164, 237
Schneider, P., & Weiss, A. 1987, A&A, 171, 49
Suzuki, D., Bennett, D. P., Udalski, A., et al. 2018, AJ, 155, 263
Udalski, A., Szymański, M., Kałużny, J., et al. 1994, Acta Astron., 44, 1
Udalski, A., Szymański, M. K., & Szymański, G. 2015, Acta Astron., 65, 1
Yee, J. C., Shvartzvald, Y., Gal-Yam, A., et al. 2012, ApJ, 755, 102
Yoo, J., DePoy, D. L., Gal-Yam, A., et al. 2004, ApJ, 603, 139
Zang, W., Han, C., Kondo, I., et al. 2021, Res. Astron. Astrophys., 21, 239